applied sciences

MDPI

Communication

Tiling Photonic Topological Insulator for Laser Applications

Petr N. Kim [1,2], Dmitry P. Fedchenko [1,2], Natalya V. Rudakova [1,2] and Ivan V. Timofeev [1,2,*]

[1] Kirensky Institute of Physics, Federal Research Center KSC SB RAS, Krasnoyarsk 660036, Russia
[2] Siberian Federal University, Krasnoyarsk 660041, Russia
* Correspondence: tiv@iph.krasn.ru

1. Supplementary Materials

Figures S1-S7 show the behavior of the beam trajectory when passing through the TPhTI.
Figures S4-S5 show a trajectory that bends around the defect in the structure of the TPhTI.
Figures S6-S7 show a trajectory that bends around the defect in the structure of the TPhTI with resonators of a different size.
Figures S8-S10 show the operation of Snell's law.
Figure S11 shows scattering matrix formalism to explain topological protection.

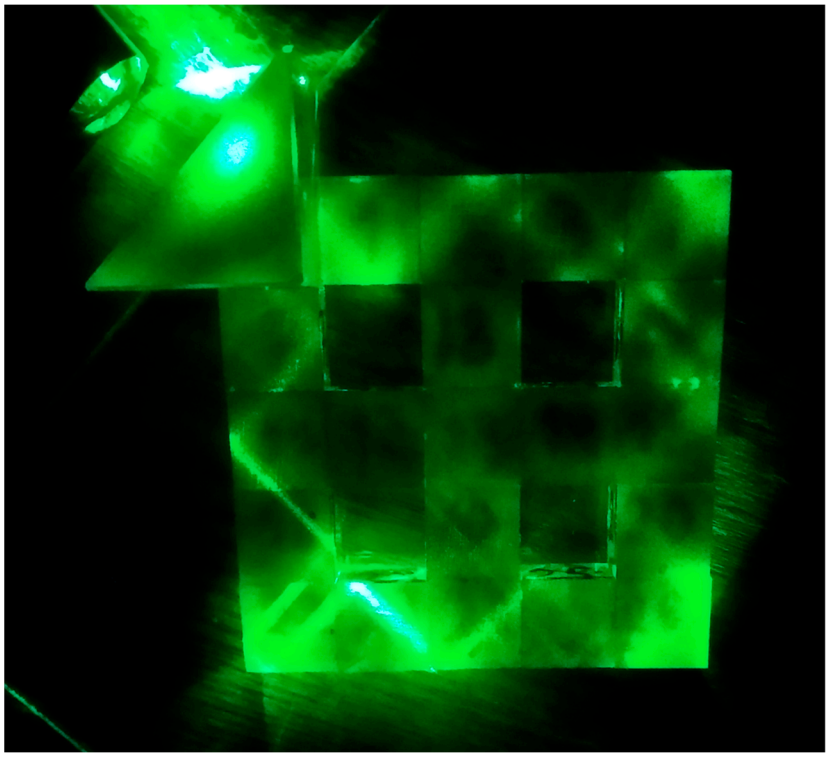

Figure S1. Beam trajectory photograph. The TPhTI composed of twenty prism resonators.

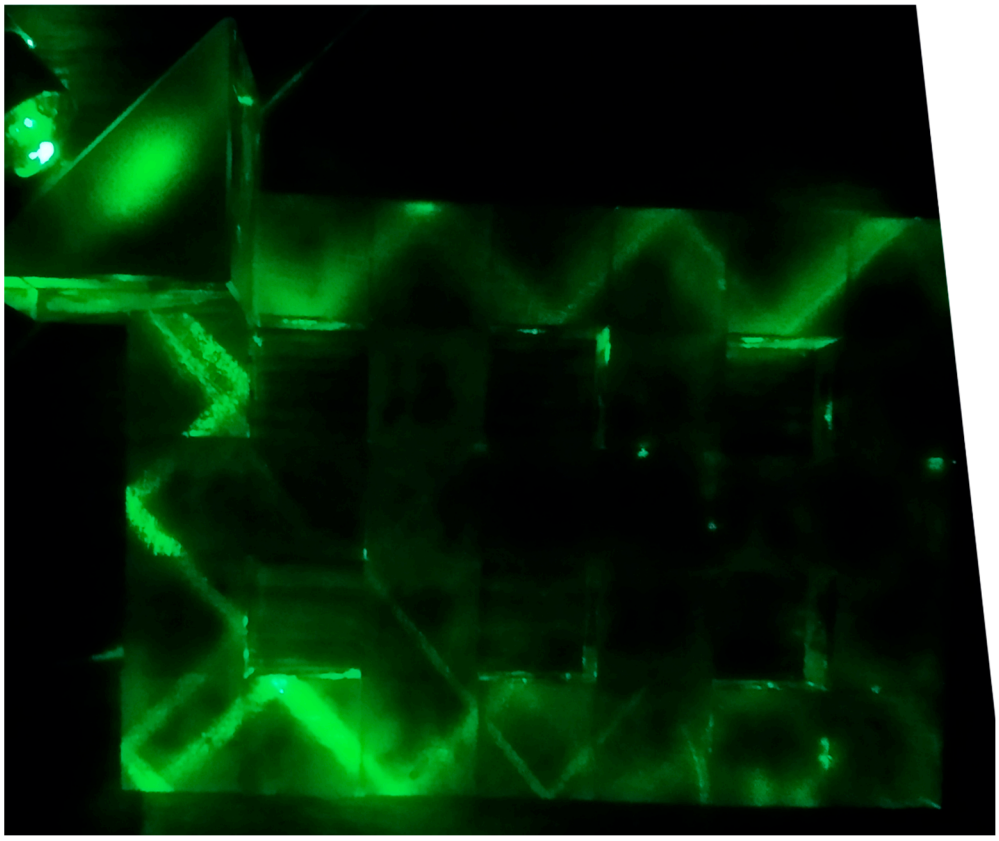

Figure S2. Beam trajectory photograph. The beam trajectory inside the smooth TPhTI.

Figure S3. Beam trajectory photograph. The TPhTI composed of twelve prism resonators.

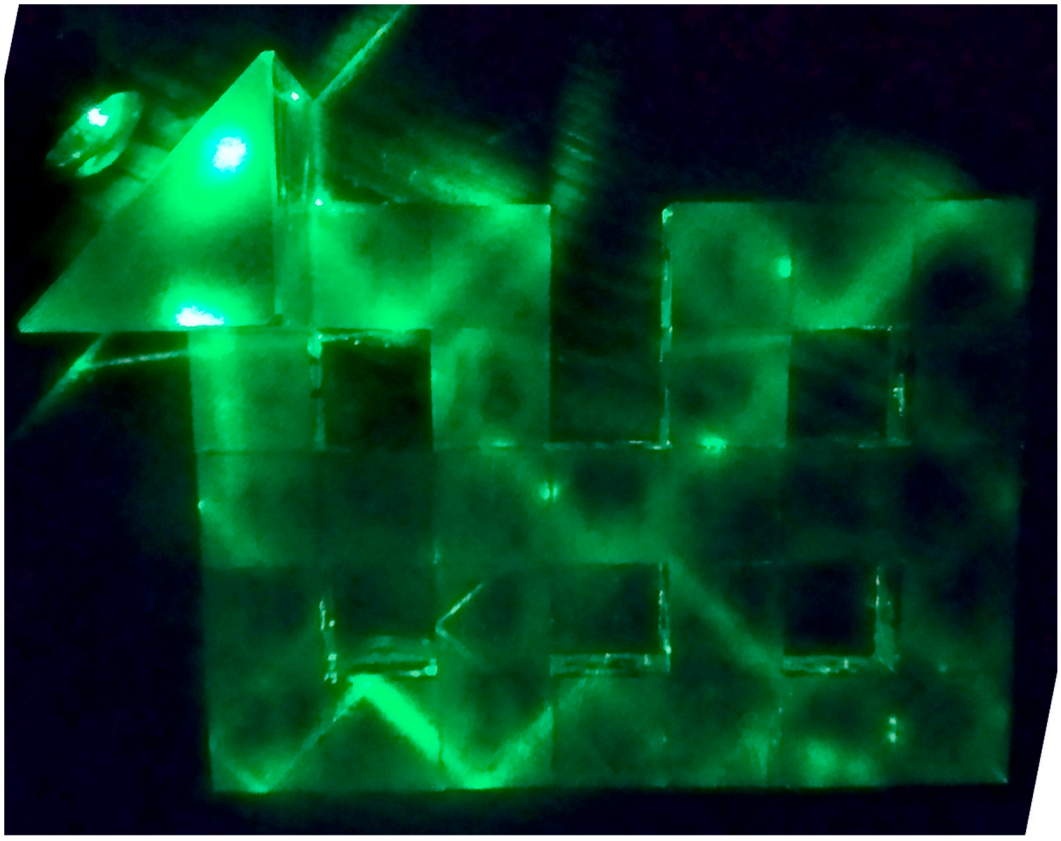

Figure S4. Beam trajectory photograph. The corrected trajectory inside the TPhTI without the prism resonator #3 as denoted in Figure 1b. The photograph shows that the light beam successfully bends around the defect of TPhTI tiling.

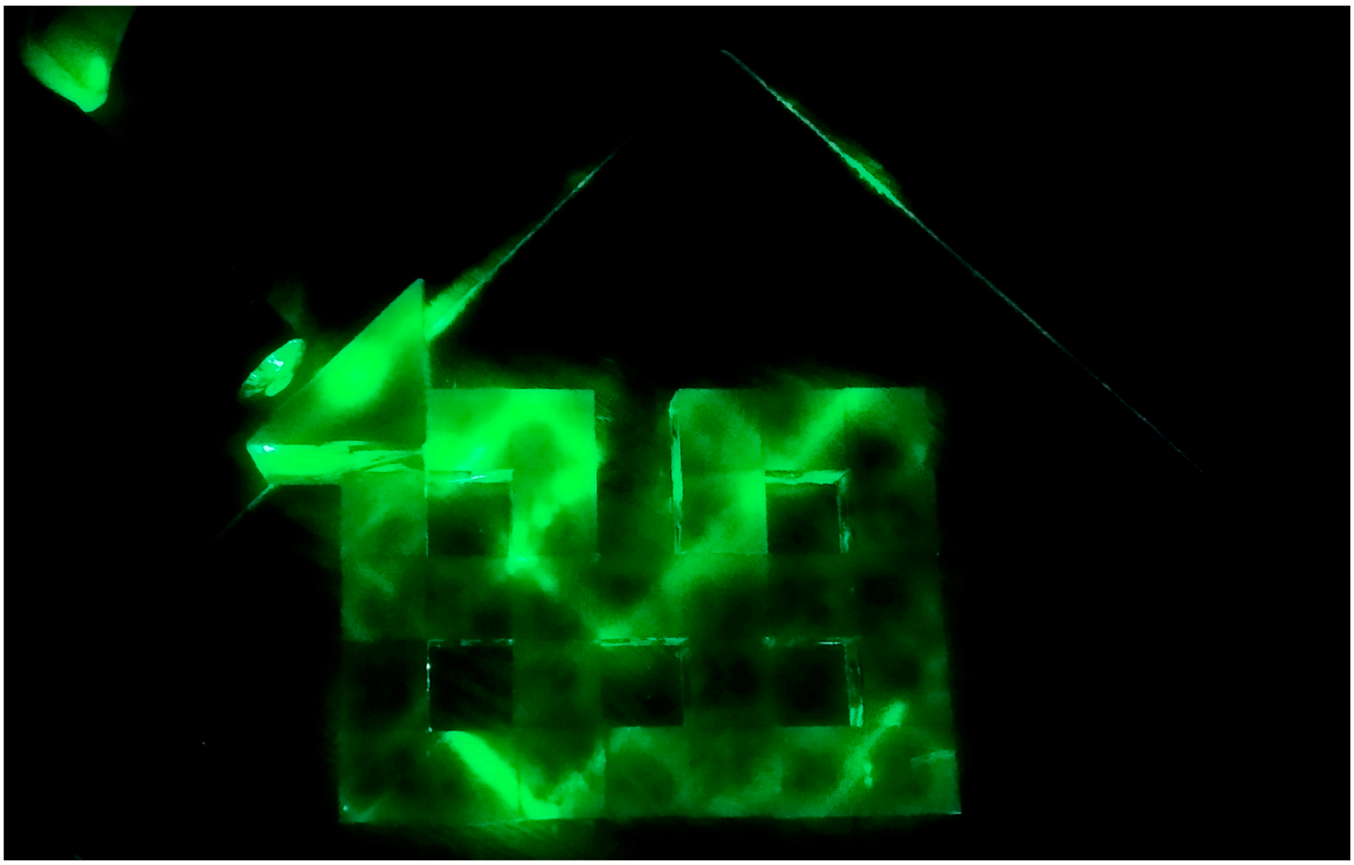

Figure S5. Beam trajectory photograph. The corrected trajectory inside the TPhTI without the prism resonator #3 as denoted in Figure 1b. The photograph shows that the light beam successfully bends around the defect of TPhTI tiling. The beam trajectory passes along the surface of the TPhTI structure due to the effect of total internal reflection on the faces of the prism resonators and exits back, as evidenced by the bright spot in the upper left corner of Figure S5.

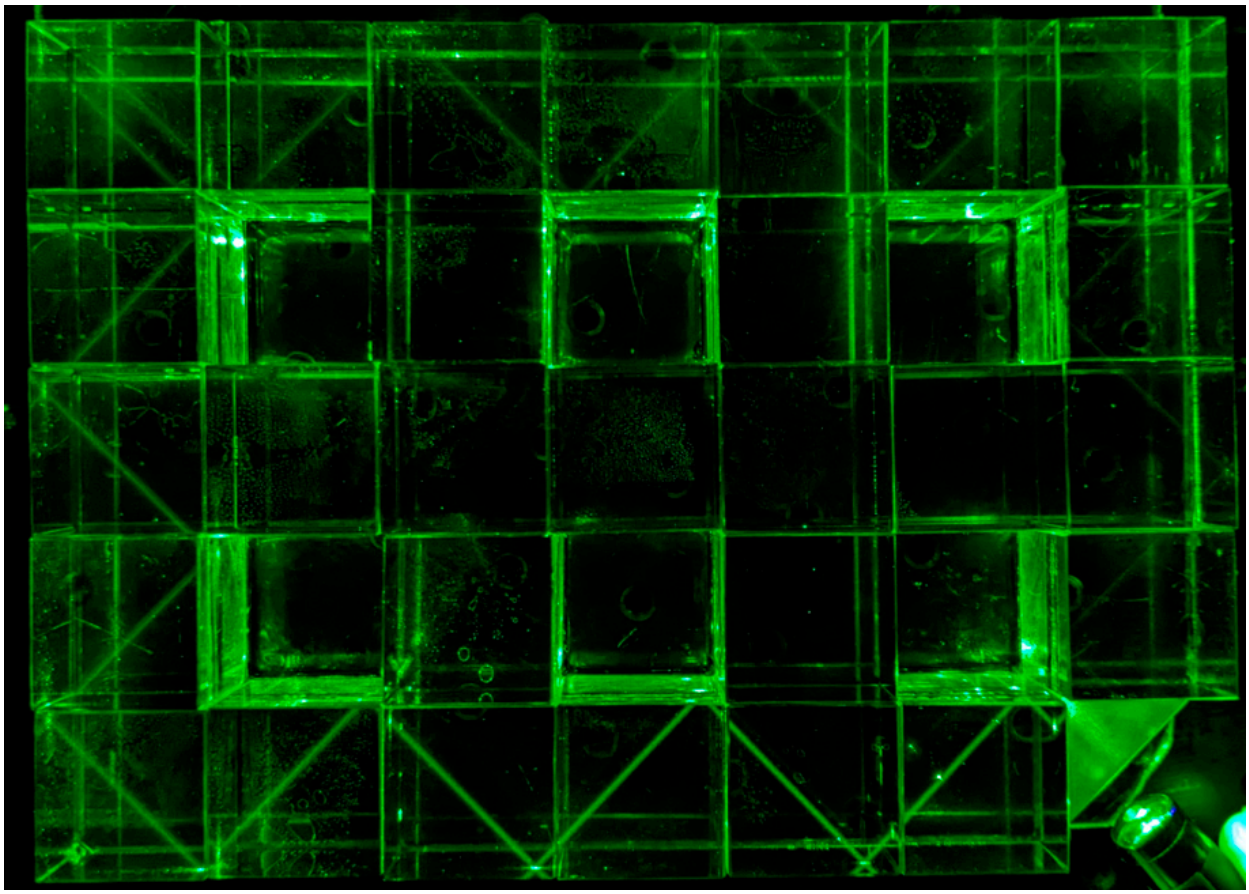

Figure S6. Beam trajectory photograph. The TPhTI composed of twenty prism resonators with dimensions 30×30×30 mm^3**.**

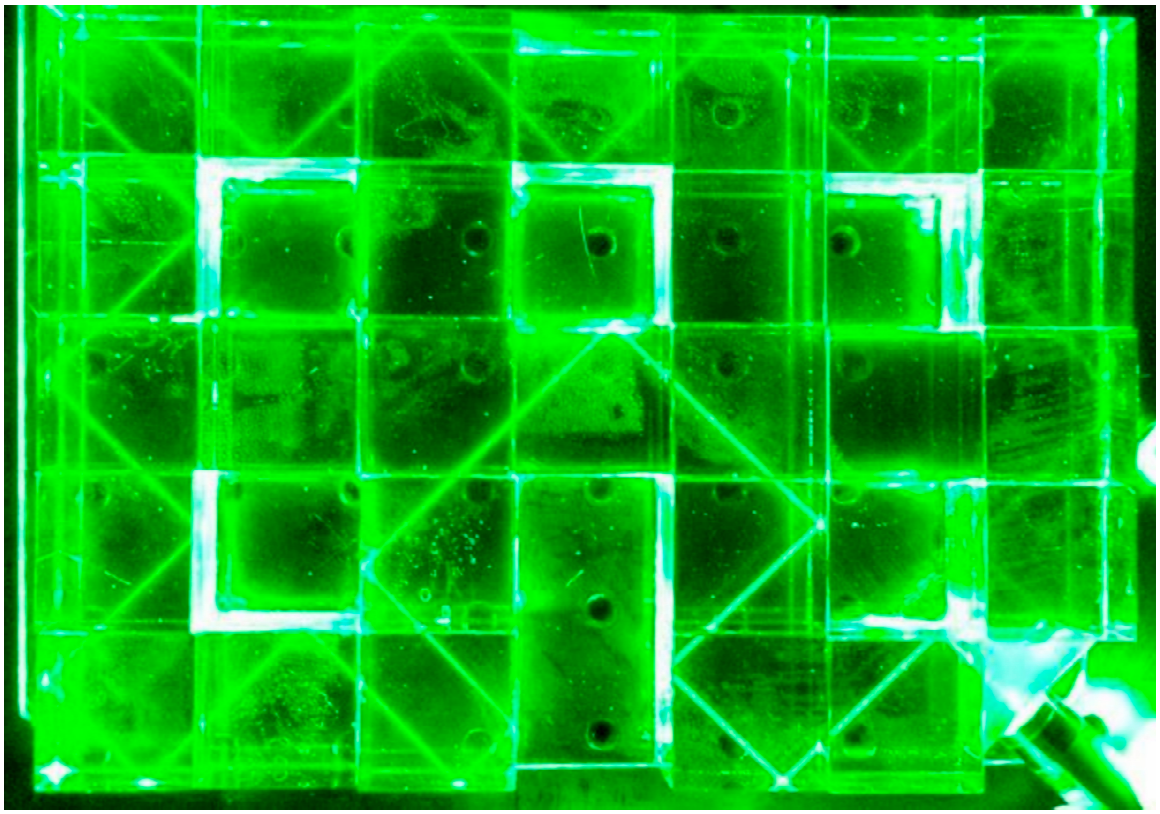

Figure S7. Beam trajectory photograph. The corrected trajectory inside the TPhTI without the prism resonator #3 as denoted in Figure 1b. The photograph shows that the light beam successfully bends around the defect of TPhTI tiling. The beam trajectory passes along the surface of the TPhTI structure due to the effect of total internal reflection on the faces of the prism resonators and exits back, even with a different size of the resonators themselves.

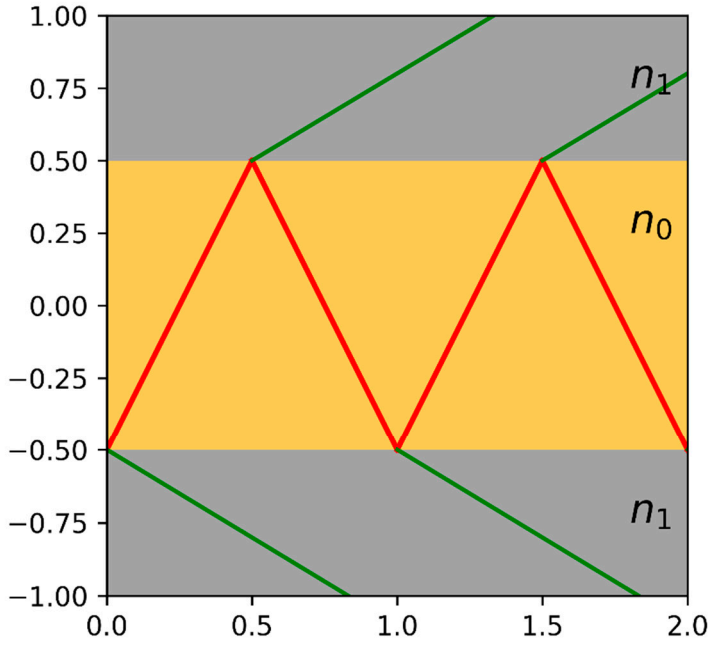

Figure S8. The behavior of the beam trajectory after reflection from the face of the prism resonator. The red color shows the reflection of the trajectory from the wall of the prism resonator. The green color shows the propagation of light in the air after refraction at the boundary of two media with refractive indices $n_1 = 1$ and $n_0 = 1.43$. The angle of incidence is 26.27°.

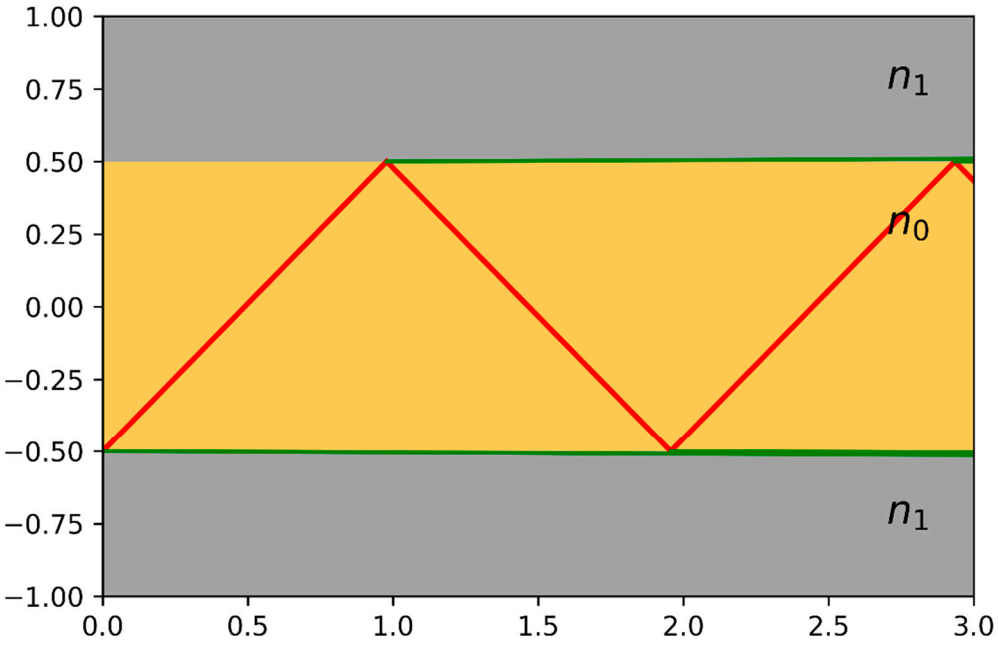

Figure S9. The behavior of the beam trajectory after reflection from the face of the prism resonator. The angle of incidence is 0.77437 radians (approximately 44.37°).

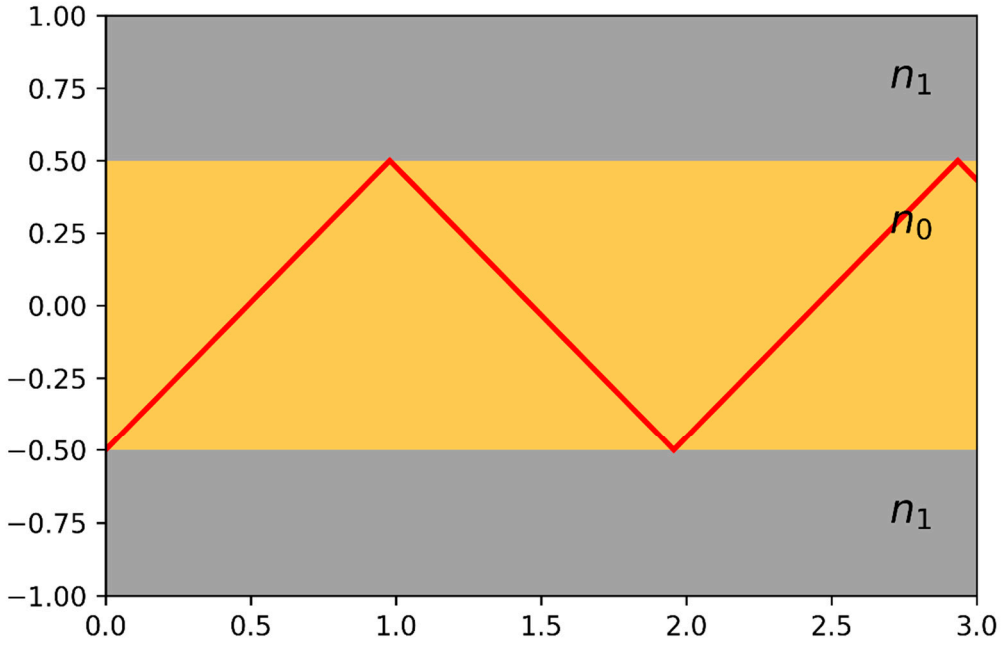

Figure S10. The behavior of the beam trajectory after reflection from the face of the prism resonator. The angle of incidence is 0.77443 radians (approximately 44.37°). The green ray disappears due to reaching a critical value for the angle of incidence, after which a complete internal reflection occurs.

Scattering matrix, Hamiltonian and topological invariant

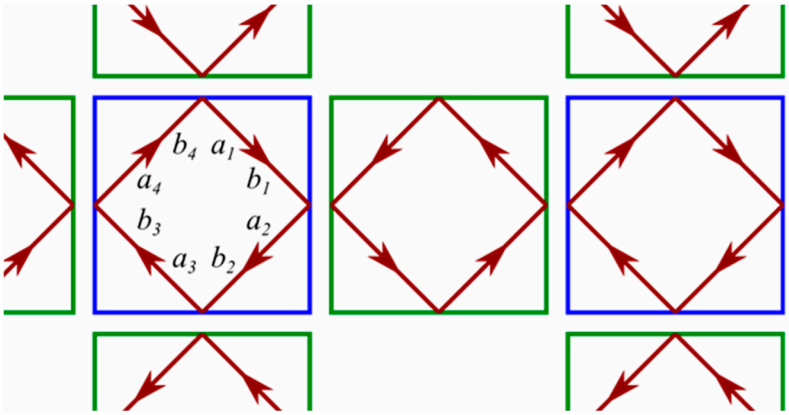

Figure S11. Scattering matrix derivation. Main prism resonators are in blue, coupling resonators are in green. Red arrows show clockwise pseudo-spin inside the resonator. Amplitudes are labeled as *a* - incoming, *b* - outgoing. Four indices correspond to +- x,y directions.

The conventional theoretical description of TPhTI is analogous to ring resonator topological insulator. The labeling of trajectory inside the prism resonator (Figure S11) exactly corresponds to [24,28,29]. The scattering matrix $\widehat{\boldsymbol{S}}$ connects the incoming light $|\boldsymbol{a}\rangle = [\boldsymbol{a_1}, \boldsymbol{a_2}, \boldsymbol{a_3}, \boldsymbol{a_4}]^{\boldsymbol{T}}$ with the outboing lingh $|\boldsymbol{b}\rangle = [\boldsymbol{b_1}, \boldsymbol{b_2}, \boldsymbol{b_3}, \boldsymbol{b_4}]^{\boldsymbol{T}}$ as $|\boldsymbol{b}\rangle = \widehat{\boldsymbol{S}}|\boldsymbol{a}\rangle$.

The crucial moment is the *phase-free approach* that relays the centimeter scale of the prism to the micrometer scale of the wavelength. A convenient illustration is the transfer matrix simulation of transmission spectra for a multilayer photonic crystal [30,31]. As usual, the micrometer size multilayer is placed above the millimeter size substrate. The substrate has two surfaces. And the distant surface between substrate and air makes considerable reflection. Remarkably, the

distantly reflected electromagnetic wave is accounted for in an exceptional way. All the other reflected waves are superposed coherently and their amplitudes are summarized. The distant wave is summarized by its *phase-free* intensity rather than the complex amplitude. The millimeter-size distance makes its impact non-coherent. The wave phase is averaged. The distant impact can be evaluated if the phase incursion is set to zero. As well, the 'frequency' and 'wave vector' can be considered zero.

In the centimeter scale of the prism resonator the wave phase is also averaged. Its frequency is stuck to zero, making a problem with the investigation of band gap topology. Nonetheless, we treat this approach as a particular case of small non-zero phase incursion *kd* for wave vector *k* at distance *d*. In this regard, the scattering inside the resonator is described by the matrix

$$\widehat{\boldsymbol{S}}_{\boldsymbol{in}} = \boldsymbol{e}^{\boldsymbol{ikd}}\,\hat{\boldsymbol{I}} = \boldsymbol{e}^{\boldsymbol{ikd}}\begin{pmatrix} \mathbf{1} & \mathbf{0} & \mathbf{0} & \mathbf{0} \\ \mathbf{0} & \mathbf{1} & \mathbf{0} & \mathbf{0} \\ \mathbf{0} & \mathbf{0} & \mathbf{1} & \mathbf{0} \\ \mathbf{0} & \mathbf{0} & \mathbf{0} & \mathbf{1} \end{pmatrix}.$$

The Bloch solution for wave vector $\widehat{\boldsymbol{K}}$ at the resonator with position $\overrightarrow{\boldsymbol{r_n}}$ has amplitudes $|\boldsymbol{a_n}, \boldsymbol{b_n}\rangle = \boldsymbol{e}^{\boldsymbol{i}\,\vec{\boldsymbol{K}}\,\overrightarrow{\boldsymbol{r_n}}}|\boldsymbol{a_0}, \boldsymbol{b_0}\rangle$. The scattering matrix of neighboring resonators $|\boldsymbol{a}\rangle = \widehat{\boldsymbol{S}}_{\boldsymbol{out}}|\boldsymbol{b}\rangle$ is:

$$\widehat{\boldsymbol{S}}_{\boldsymbol{out}} = \begin{pmatrix} \mathbf{0} & \boldsymbol{e}^{-\boldsymbol{i}\,\vec{\boldsymbol{K}}\,\vec{\boldsymbol{y}}} & \mathbf{0} & \mathbf{0} \\ \mathbf{0} & \mathbf{0} & \boldsymbol{e}^{-\boldsymbol{i}\,\vec{\boldsymbol{K}}\,\vec{\boldsymbol{x}}} & \mathbf{0} \\ \mathbf{0} & \mathbf{0} & \mathbf{0} & \boldsymbol{e}^{\boldsymbol{i}\,\vec{\boldsymbol{K}}\,\vec{\boldsymbol{y}}} \\ \boldsymbol{e}^{\boldsymbol{i}\,\vec{\boldsymbol{K}}\,\vec{\boldsymbol{x}}} & \mathbf{0} & \mathbf{0} & \mathbf{0} \end{pmatrix}$$

For the edge resonator there is no light transfer out of the resonator, so instead of $\widehat{\boldsymbol{S}}_{\boldsymbol{out}}$ the scattering $|\boldsymbol{a}\rangle = \widehat{\boldsymbol{S}}_{\boldsymbol{edge}}|\boldsymbol{b}\rangle$ is described by another matrix:

$$\widehat{\boldsymbol{S}}_{\boldsymbol{edge}} = \begin{pmatrix} \mathbf{0} & \mathbf{0} & \mathbf{0} & \mathbf{1} \\ \mathbf{1} & \mathbf{0} & \mathbf{0} & \mathbf{0} \\ \mathbf{0} & \mathbf{1} & \mathbf{0} & \mathbf{0} \\ \mathbf{0} & \mathbf{0} & \mathbf{1} & \mathbf{0} \end{pmatrix}.$$

The eigensolution obeys equation

$$\widehat{\boldsymbol{S}}_{\boldsymbol{out}}\widehat{\boldsymbol{S}}_{\boldsymbol{in}}|\boldsymbol{a}\rangle = \boldsymbol{e}^{\boldsymbol{i\phi}}|\boldsymbol{a}\rangle. \quad (1)$$

One can notice than

$$|\boldsymbol{a}\rangle = \widehat{\boldsymbol{S}}_{\boldsymbol{out}}|\boldsymbol{b}\rangle = \widehat{\boldsymbol{S}}_{\boldsymbol{out}}\widehat{\boldsymbol{S}}_{\boldsymbol{in}}|\boldsymbol{a}\rangle = \left(\widehat{\boldsymbol{S}}_{\boldsymbol{out}}\widehat{\boldsymbol{S}}_{\boldsymbol{in}}\right)^{\mathbf{4}}|\boldsymbol{a}\rangle = \hat{\boldsymbol{I}}|\boldsymbol{a}\rangle,$$

that is valid for arbitrary wave vector. In the gapless insulator the flat band has zero group velocity $\frac{\boldsymbol{\partial\omega}}{\boldsymbol{\partial k}} = \mathbf{0}$ [17]. Physically it means that in the bulk each photon circulates between four main resonators and the energy does not penetrate through the array.

Note 1. Hamiltonian. The analogous scattering matrix can be constructed for the honeycomb network. When the weak nearest-neighbor coupling is taken into account, the description is analogous to Dirac tight binding Hamiltonian of graphene, see Appendix B in [28]. For the experimental situation the coupling between prism resonators is strong. So, it is more appropriate to obtain an effective Hamiltonian by taking the matrix logarithm of Eq. (1).

Note 2. Topological invariant. The existence of edge solution suggests to apply *bulk-edge correspondence* as it was made for the equivalent Rudner toy [17]. Here the Chern number of each band is zero, so Rudner and coauthors use homotopy-class-based topological invariants, such as "$\boldsymbol{\nu_{1,3}}$ invariants". The TPhTI uses the same approach, but the only experimentally possible situation is for zero frequency (quasi-energy).

Note 3. Topologically trivial case. It is a conventional routine to compare the presented topologically non-trivial case with the trivial one. This purpose requires to vary the coupling strength in $\widehat{\boldsymbol{S}}_{\boldsymbol{out}}$ [28]. Some portion of light has to be reflected back into the resonator, and the reflected light has to interfere with the transmitted one. In phase-free approach it is hard to reach this experimentally because of a coherence problem.

Measurement procedure

The intensity of the laser beam that passes through the TPhTI was measured with a light meter assembled on the basis of a photoresistor. The resistance depends on the illumination level. The logarithmic dependence is linearized to the scale of lux units. The lux meter was placed at a certain distance from the array so that the beam path outside the array and the angle of incidence of the beam on the photoresistor were fixed. The laser was oriented to make the beam spot fall exactly at the photoresistor eye center. The maximum value shown by the luxmeter was averaged between 4 measurements.

References

1. Bandres, M.A.; Wittek, S.; Harari, G.; Parto, M.; Ren, J.; Segev, M.; Christodoulides, D.N.; Khajavikhan, M. Topological insulator laser: Experiments. Science 2018, 359, eaar4005.
2. Harari, G.; Bandres, M.A.; Lumer, Y.; Rechtsman, M.C.; Chong, Y.D.; Khajavikhan, M.; Christodoulides, D.N.; Segev, M. Topological insulator laser: Theory. *Science* **2018**, *359*, eaar4003.
3. Zeng, Y.; Chattopadhyay, U.; Zhu, B.; Qiang, B.; Li, J.; Jin, Y.; Li, L.; Davies, A.G.; Linfield, E.H.; Zhang, B.; et al. Electrically pumped topological laser with valley edge modes. *Nature* **2020**, *578*, 246–250.
4. Dikopoltsev, A.; Harder, T.H.; Lustig, E.; Egorov, O.A.; Beierlein, J.; Wolf, A.; Lumer, Y.; Emmerling, M.; Schneider, C.; Höfling, S.; et al. Topological insulator vertical-cavity laser array. *Science* **2021**, *373*, 1514–1517.
5. Shao, Z.-K.; Chen, H.-Z.; Wang, S.; Mao, X.-R.; Yang, Z.-Q.; Wang, S.-L.; Wang, X.-X.; Hu, X.; Ma, R.-M. A high-performance topological bulk laser based on band-inversion-induced reflection. *Nat. Nanotechnol.* **2020**, *15*, 67–72.
6. Yang, Z.-Q.; Shao, Z.-K.; Chen, H.-Z.; Mao, X.-R.; Ma, R.-M. Spin-Momentum-Locked Edge Mode for Topological Vortex Lasing. *Phys. Rev. Lett.* **2020**, *125*, 013903.
7. Schomerus, H. Topologically protected midgap states in complex photonic lattices. *Opt. Lett.* **2013**, *38*, 1912.
8. St-Jean, P.; Goblot, V.; Galopin, E.; Lemaître, A.; Ozawa, T.; Le Gratiet, L.; Sagnes, I.; Bloch, J.; Amo, A. Lasing in topological edge states of a one-dimensional lattice. *Nat. Photon.* **2017**, *11*, 651–656.
9. Parto, M.; Wittek, S.; Hodaei, H.; Harari, G.; Bandres, M.A.; Ren, J.; Rechtsman, M.C.; Segev, M.; Christodoulides, D.N.; Khajavikhan, M. Edge-Mode Lasing in 1D Topological Active Arrays. *Phys. Rev. Lett.* **2018**, *120*, 113901.
10. Ishida, N.; Ota, Y.; Lin, W.; Byrnes, T.; Arakawa, Y.; Iwamoto, S. A large-scale single-mode array laser based on a topological edge mode. *Nanophotonics* **2022**, *11*, 2169–2181.
11. Hasan, M.Z.; Kane, C.L. Colloquium: Topological insulators. *Rev. Mod. Phys.* **2010**, *82*, 3045–3067.
12. Thouless, D.J.; Kohmoto, M.; Nightingale, M.P.; den Nijs, M. Quantized Hall conductance in a two-dimensional periodic potential. *Phys. Rev. Lett.* **1982**, *49*, 405.
13. Cheng, X.; Jouvaud, C.; Ni, X.; Mousavi, S.H.; Genack, A.Z.; Khanikaev, A.B. Robust reconfigurable electromagnetic pathways within a photonic topological insulator. *Nat. Mater.* **2016**, *15*, 542–548.
14. Haldane, F.D.M.; Raghu, S. Possible Realization of Directional Optical Waveguides in Photonic Crystals with Broken Time-Reversal Symmetry. *Phys. Rev. Lett.* **2008**, *100*, 013904.
15. Mong, R.S.K.; Shivamoggi, V. Edge states and the bulk-boundary correspondence in Dirac Hamiltonians. *Phys. Rev. B* **2011**, *83*, 125109.
16. Khanikaev, A.B.; Shvets, G. Two-dimensional topological photonics. *Nat. Photonics* **2017**, *11*, 763–773.
17. Rudner, M.S.; Lindner, N.H.; Berg, E.; Levin, M. Anomalous Edge States and the Bulk-Edge Correspondence for Periodically Driven Two-Dimensional Systems. *Phys. Rev. X* **2013**, *3*, 031005.
18. Leykam, D.; Yuan, L. Topological phases in ring resonators: recent progress and future prospects. *Nanophotonics* **2020**, *9*, 4473–4487.
19. Fedchenko, D.P.; Kim, P.N.; Timofeev, I.V. Photonic Topological Insulator Based on Frustrated Total Internal Reflection in Array of Coupled Prism Resonators. *Symmetry* **2022**, *14*, 2673.
20. Yang, Z.; Lustig, E.; Harari, G.; Plotnik, Y.; Lumer, Y.; Bandres, M.A.; Segev, M. Mode-Locked Topological Insulator Laser Utilizing Synthetic Dimensions. *Phys. Rev. X* **2020**, *10*, 011059.
21. Liu, Y.G.N.; Wei, Y.; Hemmatyar, O.; Pyrialakos, G.G.; Jung, P.S.; Christodoulides, D.N.; Khajavikhan, M. Complex skin modes in non-Hermitian coupled laser arrays. *Light Sci. Appl.* **2022**, *11*, 336.
22. Liu, Y.G.N.; Jung, P.S.; Parto, M.; Christodoulides, D.N.; Khajavikhan, M. Gain-induced topological response via tailored long-range interactions. *Nat. Phys.* **2021**, *17*, 704–709.
23. Maksutov, D.D. New Catadioptric Meniscus Systems. *J. Opt. Soc. Am.* **1944**, *34*, 270.

24. Gao, F.; Gao, Z.; Shi, X.; Yang, Z.; Lin, X.; Xu, H.; Joannopoulos, J.D.; Soljačić, M.; Chen, H.; Lu, L.; Chong, Y. Probing topological protection using a designer surface plasmon structure. *Nat. Commun.* **2016**, *7*, 11619.
25. Grushevskaya, H.V.; Krylov, G.G.; Kruchinin, S.P.; Vlahovic, B.; Bellucci, S. Electronic properties and quasi-zero-energy states of graphene quantum dots. *Phys. Rev. B* **2021**, *103*, 235102.
26. Farrelly, T. A review of quantum cellular automata. *Quantum* **2020**, *4*, 368.
27. Li, M.; Zhirihin, D.; Gorlach, M.; Ni, X.; Filonov, D.; Slobozhanyuk, A.; Alù, A.; Khanikaev, A.B. Higher-order topological states in photonic kagome crystals with long-range interactions. *Nat. Photon.* **2020**, *14*, 89–94.
28. Pasek, M.; Chong, Y.D. Network models of photonic Floquet topological insulators. *Phys. Rev. B—Condens. Matter Mater. Phys.* **2014**, *89*, 075113.
29. Shalaev, M.I.; Walasik, W.; Tsukernik, A.; Xu, Y.; Litchinitser, N.M. Robust topologically protected transport in photonic crystals at telecommunication wavelengths. *Nat. Nanotechnol.* **2019**, *14*, 31–34.
30. Joannopoulos, J.; Johnson, S.; Winn, J.; Meade, R.D. *Photonic Crystals: Molding the Flow of Light*, 2nd ed.; Princeton University: Princeton, NJ, USA, 2008; p. 305.
31. Vetrov, S.Y.; Timofeev, I.V.; Shabanov, V.F. Localized modes in chiral photonic structures. *Physics-Uspekhi* **2020**, *63*, 33.